PNAS
www.pnas.org

Supplementary Information for

Continuous-range tunable multi-layer frequency selective surfaces using origami and inkjet-printing

Syed Abdullah Nauroze, Larissa S. Novelino, Manos M. Tentzeris and Glaucio H. Paulino

Glaucio H. Paulino.
E-mail: paulino@gatech.edu

This PDF file includes:

Supplementary text
Figs. S1 to S10
Tables S1 to S2
Captions for Movies S1 to S3
References for SI reference citations

Other supplementary materials for this manuscript include the following:

Movies S1 to S3

www.pnas.org/cgi/doi/10.1073/pnas.1812486115

Supporting Information Text

1. Miura-Ori Geometry

The Miura-Ori is a rigid foldable origami tessellation defined by the geometry of its rhombic-shaped panels, each of which is characterized by the two lengths a and b and the acute angle α. This pattern presents one degree of freedom, meaning that we describe its kinematics by one of the dihedral angles between panels, defined as the folding angle. Our parametrization for the Miura-Ori unit cell follows (1), where θ is used as folding angle (Fig. S1):

$$w = 2b\xi, \quad \ell = 2a\zeta, \quad v = b(1-\xi^2)^{1/2}, \quad h = a\zeta tan(\alpha)cos(\theta/2) \tag{S1}$$

where

$$\xi = sin(\alpha)sin(\theta/2), \quad \zeta = cos(\alpha)(1-\xi^2)^{-1/2} \tag{S2}$$

In addition, the dihedral angle φ (Fig. S1), which is the dihedral angle between the folded dipoles, is also expressed as a function of θ,

$$\varphi = 2\sin^{-1}(\zeta \sin(\theta/2)) \tag{S3}$$

Multiple layers of the Miura-Ori pattern with compatible in-plane kinematics can be stacked. This compatibility is achieved if the dimensions w, ℓ and v are the same for all the layers, leaving h as an independent dimension (2, 3) (Fig. S1). Those conditions result in the design constraints on Eq. S4.

$$a_t = a_b \frac{cos(\alpha_b)}{cos(\alpha_t)}, \quad b_t = b_b \tag{S4}$$

where, the subscript b and t represent the bottom and top layer a given Miura design parameter. In addition, because the stacking preserves the in-plane kinematics, a single dihedral angle can still be used to describe the kinematics of the stacking, thus the folding angle θ_t of the top layer can be written in terms of the bottom layer

$$sin(\theta_t/2) = \frac{sin(\alpha_b)}{sin(\alpha_t)} sin(\theta_b/2) \tag{S5}$$

Multi-layer structures retain the flat-foldability of the Miura-Ori, that is, they can still be fully folded (i.e, folding angles $\theta_t = \theta_b = 0$). However, structures with distinct layers have the total extension of the largest layer limited by the smallest layer.When the smallest layer is fully extended ($\theta = 180°$), all the other layers will be restrained to further expansion and that will be the maximum expansion of those. Therefore, a Miura-Ori with layers with distinct geometry cannot be unfolded into a flat configuration, but it is still flat-foldable. The maximum folding angle of each layer is defined by

$$\theta_t = 2sin^{-1}\left(\frac{sin(\alpha_b)}{sin(\alpha_t)}\right) \tag{S6}$$

The design constraints on Eq. S4 and the relationship between folding angles on Eq. S5 are valid for both types of stacking. For inline stacking, we followed the Eq. S4 to design compatible top layers for a bottom layer with fixed intrinsic geometry $a_b = 20$ mm, $b_b = 20$ mm and $\alpha_b = 45°$. On Table S1, we report the length a_t of the panel for each panel angle α_t studied in this work. For the mirror stacking, we used identical layers, therefore the design constraints are automatically satisfied. While in theory the mirror stacking and the bottom layer of the inline stacking are able to completely unfold, in practice, for the paper prototype, this unfolding is not trivial because of the plasticity of paper at the hinges. However, this plasticity acts in our favor because it allows the pattern to keep the angle engaged (i.e. retains the mountain and valley assignment, which is fundamental for the pattern actuation. (Fig. S2). It is important to notice that, the use of other materials as substrate and other approaches to create hinges are possible, in which the complete unfolding is achievable.

The distances between conductor elements, D_w and D_ℓ, changes with the folding angle θ and these can be expressed in terms of the parameters w and ℓ of the unit cell, the length of the conductor line l_c, and the line position within the unit cell.

$$D_w = \beta w, \quad D_\ell = \psi \ell \tag{S7}$$

where $\psi = \ell_c/2a$ and β is the design parameter that provides the conductor position in the unit cell (Fig. S1). When considering multi-layer structures, the extrinsic parameters w and ℓ on Eq. 9 are expressed in terms of the bottom layer parameters (i.e., a_b, b_b, α_b), while β and ψ refers to the specific layer where the conducts are located. For multi-layer configurations, the interlayer distance is defined by an extra extrinsic parameter Δh. For the in-line stacking, this is expressed as

$$\Delta h = h_t - h_b \tag{S8}$$

and for the mirror stacking

$$\Delta h = h_t + h_b \tag{S9}$$

where for identical layers, $\Delta h = 2h_b$.

2. Mechanical Analysis

To simulate the electromagnetic response of the Miura-FSS structure, we assumed that the Miura-Ori has a rigid origami behavior. The following mechanical analysis shows that this is a fair assumption for the proposed structure Fig. S3

A. Bar and Hinge Simulation. We discretized the unit cells according to the bar and hinge model (4). This reduced-order model represents the vertices by pin-joints and the fold lines by bars with axial stiffness and rotational springs along them. In addition, to avoid internal mechanisms and to give an approximation to the bending of the panels, the panels are triangulated by similar bar elements (Fig. S3(A). The most important parameter for such analysis is the ratio k_r between the bending stiffness (k_{bend}) of the panels and the folding stiffness of the hinges (k_{fold}). Therefore, we tested the cellulose paper used to fabricate the Miura-FSS, and obtained this ratio equal to 3.3 (see subsection 2.B). Using the bar and hinge model and the obtained stiffness ratio, we simulated the in-plan motion of the Miura-FSS using the Merlin software (5–7), a MATLAB implementation that simulates the mechanical behavior of origami structures using a non-linear formulation.

To simulate the same folding motion necessary for the reconfigurability of the proposed Miura-FSS, we applied the boundary conditions shown in Fig. S3(B) and imposed the displacement of the boundary nodes on the right. The total imposed displacement was computed such that it was equivalent to the change in folding angle from $\theta = 120^\circ$ to $\theta = 60^\circ$ (i.e., displacement of -62.12 in the x-direction). The final configuration, equivalent to $\theta = 60^\circ$ is shown in Fig. S3C, where the brown lines represent the initial configuration. Figure S3(D-E) shows the final configuration obtained from the simulation for single-layer, mirror and inline stacking, where the red lines represent the position of the crease lines under a rigid origami assumption, (i.e. calculated following the parametrization in Eq. S1). We observed that the unit cells that are in the boundary clearly do not behave as rigid origami, but the unit cells in the middle present a behavior close to a rigid fold origami. Thus, in Fig. S3 (G-I), we quantitatively compare the values for the parameters calculated from Eq. S1 and Eq. S3 (red column) with the parameters measured for each unit cell. The green and blue columns represent the minimum and maximum values obtained from the Merlin simulation, respectively. The percentages indicate the difference between the values obtained from the simulation and the values from Eqs. S1 and S3.

Fig. S3 (J-L) shows the stored energy, where the red line is the total stored energy. The shaded areas in red, blue and magenta represent the portion of energy of the hinge folding, panels bending and stretching of the crease lines, respectively. We observe that for the single-layer a small portion of the energy correspond to bending and stretching, while for the multi-layer structures those are negligible.

B. Mechanical Properties of the Paper. To obtain the stiffness of the paper at the panels and at the hinges, we emulate the bending of a single panel and the folding of a single hinge made of cellulose paper of thickness 0.11 mm. For the measurement of the bending stiffness, we tested a single panel with dimensions 40x20 mm, surrounded by folded tabs. Those tabs simulate the existence of the surrounding panels. We attached one side of the panel to the support, and applied a total displacement 5 mm along the z-direction (see Fig. S4A). To apply this displacement, we use an arm located 20 mm (in the y-direction) from the support. This arm is attached to a load cell, that measures the reaction force (F).

For the measurement of the folding stiffness, we tested five samples with two 20x20 mm panels. Those Panels are also surrounded by folded tabs and are connected by a single hinge that was fabricated with the same dashed perforation as the Miura-FSS samples. The hinge was completely folded before the test and unfolded to the configuration shown in Fig. S4, where $d_{x0} = 5$ mm. For the testing, similarly to the panels test, we attached the sample to the support and applied a total displacement (in the x-direction) of 10 mm uniform along the z-direction using an arm located 20 mm from the support.

For each increment of applied displacement (Δd_x) and measured force (F), we calculate the moment M at the bending/folding regions and the rotation angle ρ as

$$M = d_x F, \quad \rho = \tan^{-1}\left(\frac{d_{x0}}{d_y}\right) - \tan^{-1}\left(\frac{d_{x0} - \Delta d_x}{d_y}\right) \qquad [S10]$$

and we plotted the moment-rotation curve shown in Fig. 10. From the slope of the fitted curve, we obtained the stiffness of each sample. In Table S2 we show the stiffness per unit length for each sample. We average the stiffness values and obtained the stiffness ratio $k_r = 3.3$.

3. Experimental Setup

The measurement setup used to verify the simulation results consisted of a customized Miura-FSS sample holder with an integrated 3D-printed frame, which was placed in the middle of two constant gain horn antennas as shown in Fig. S5. The antennas were placed in line-of-sight of each other to realize maximum power transfer between them and were connected to a vector network analyzer (VNA) using coaxial cables. The distance between the two antennas was kept far enough such that the Miura-FSS sample was in far-field of each antenna, this is a key criterion for an FSS measurement to ensure that it is excited by a plane wave.

It is also important to note here that the fabricated Miura-FSS structure comprised of finite number of unit cells (hence finite FSS size) as opposed to the simulation setup, in which infinite array was assumed. Therefore, the fabricated Miura-FSS was made large enough such that it encloses the main beam of the antenna thereby mitigating the edge effects introduced by a finite FSS and realizing constant current distribution along resonant elements in the same fashion as in an infinite FSS (8).

One of the key challenges for the measurements of a Miura-FSS is to ensure that each Miura unit cell features the same folding angle. This was realized by using a 3D-printed frame for each folding angle (i.e. $\theta = 60^\circ, 90^\circ, 120^\circ$) as shown in Fig. S5. Moreover, the 3D-printed frame along with the Miura-FSS sample was secured firmly to the rotating table so that the Miura-FSS sample was parallel to the antenna aperture for normal incidence and excited by plane waves. Finally, measurements for different angles of incidence (AoI) were made by rotating the FSS structure around y-axis as shown in Fig. S5.

In this work, a two-step calibration was performed to incorporate system errors and shift the reference plane to the surface of the Miura-FSS structure. First, the effects of the VNA and coaxial cables were eliminated by using a conventional 2-port Short-Open-Load-Through (SOLT) calibration technique at the end of the coaxial cables that would be connected to the antennas. Next, a free-space Gate-Reflect-Line (GRL) calibration was performed to de-embed the region between the antennas and Miura-FSS structure. This was done by first finding the location of the Miura-FSS in time domain by comparing the return loss (as a function of time) of an empty sample holder with a metal sheet using the VNA. Then a proper time-domain gated function (according to the width of the reflected pulse) was applied to filter out any unwanted reflections. Therefore, making sure that the Miura-FSS structure was only excited by direct line-of-sight plane waves. Finally, the calibration was completed by taking reflect and line measurements by respectively placing and replacing a metal sheet with given thickness on sample holder. The quality of calibration was further improved by placing absorbers around the measurement setup to mitigate the effect of unwanted reflections from objects in its surroundings as shown in Fig. S5.

4. Finite element analysis

The Miura-FSS structures were designed and simulated using Ansys HFSS - a finite element method based software. In our simulations, we exploited the periodic nature of the Miura-FSS structure; hence we simulated a unit cell with a master/slave boundary conditions with Floquet port excitation (shown in Fig. S6A) to emulate an infinite structure, thereby saving computational time and resources. This configuration utilizes Floquet's theorem to calculate infinite periodic structures by enforcing the electric field at the master boundary to be same as the slave boundary with a phase delay. Thus, we can use the solution for a unit cell to calculate electromagnetic behavior of the whole structure by multiplying it with appropriate phase difference.

For the single-layer and mirror-stacked structures, unit cells with $a = b = 20$ mm and $\alpha = 45^\circ, 56^\circ, 60^\circ, 64^\circ, 70^\circ$ were modeled and simulated. For inline-stacked structures, the bottom unit cell has $a_b = b_b = 20$ mm and $\alpha = 45^\circ$, and the top unit cell has $b_t = 20mm$ and α_t and a_t as shown on Table S1. All the material parameters, as well as the geometric parameters are consistent with the ones utilized in the tested prototypes. For all the simulated Miura-FSS unit cells, the conductor lines were modeled with length $l_c = 20$ mm, width 2 mm, thickness 50 μm. In addition, the line position within the Miura-Ori unit cell was defined for $\beta = 0.5$ and $\gamma = 0.5$ (Fig. S1). In the model, the conductors substrate was also included, which is a cellulose paper with thickness 110 μm and relative permitivity $\varepsilon_r = 3.4$.

The simulated domain (show in Fig. S6(A)) was discretized using tetrahedron elements with first order tangential element basis functions, which have 20 degree of freedom (2 unknowns per edge and 2 unknowns per face) per tetrahedron and consider that the electric field varies linearly along the edges. The tangential components of the E-field are stored at the edges and faces of the tetrahedral elements (shown in Fig. S6(B)), and the field inside each tetrahedron is interpolated from these values such that it satisfies the following wave equation.

$$\nabla \times \left(\frac{1}{\mu_r} \nabla \times \mathbf{E}(x, y, z) \right) - k_0^2 \epsilon_r \mathbf{E}(x, y, z) = 0 \qquad [S11]$$

where,

- $\mathbf{E}$(x,y,z) is the electric field in terms of the basis functions
- μ_r and e_r are relative permeability and permitivity of the material, respectively
- k_0 and ω are phase constant of free space and angular frequency, respectively.

The tetrahedrons have their initial size determined by the relative permitivity of the material and the operating frequency. That is, each edge of the tetrahedron is set to the effective wavelength of the wave in the given material ($= \frac{1}{3f\sqrt{e_r}}$). The mesh is interactively refined by the software until convergence is achieved, which occurs when the computed E-field achieves a maximum difference of 0.02dB of scattering parameters between two consecutive iterations.

5. Equivalent-circuit model

Typically, the response of a single-layer or multi-layer FSS is evaluated using 3-D full wave simulators like HFSS and CST. However, they require higher computational power and give limited insight into the working of the structure. Therefore, equivalent-circuit models have been developed that approximate the electromagnetic behavior of the FSS structure as a network of lumped components.

In order to derive the equivalent circuit of an arbitrarily shaped FSS, we first start with the impedance of the FSS that can be represented as (9):

$$Z_{FSS} = -j \frac{\sum_{p=-\infty}^{+\infty} \sum_{q=-\infty}^{+\infty} \tilde{J}^*(p,q)\tilde{\bar{\bar{G}}}(p,q)\tilde{J}(p,q)}{2\tilde{J}^*(0,0)\tilde{\bar{\bar{G}}}(0,0)\tilde{J}(0,0)} \qquad [S12]$$

where asterisk denotes the complex conjugate and tilde presents the Fourier transform, $\tilde{\bar{\bar{G}}}$ is the dyadic Green's function in free space with infinite periodic boundary conditions, *(p,q)* are the Floquet modes and J is the current flowing through the resonant element. It can be seen that Z_{FSS} satisfies the Foster theorem (10, 11) thereby featuring the same pole-zero behavior as an LC network.

The FSS reactance values using Eq. S12 assumes that the current density for the FSS element are known as a priori. However, a simpler approach involves using a full-wave simulation to determine the reflection coefficient of the FSS structure, then use eq. S13 to determine the impedance of the freestanding FSS.

$$Z_{FSS} = -\frac{Z_0^2(1+\Gamma)}{2Z_0\Gamma} \qquad [S13]$$

where Γ and Z_0 represents the reflection coefficient and the characteristic impedance of free-space (vacuum), respectively. According to Eq. S13, the impedance of a freestanding FSS structure is purely imaginary. The dielectric losses can be incorporated by adding a series resistance in the equivalent circuit. However, these losses can be ignored if the dielectric thickness is very small as compared to the resonant frequency (12).

The structure and the number of the lumped components for an equivalent-circuit model depends on the shape of the resonant elements and their inter-elements distances. For example, a conventional 2D planar dipole-based FSS exhibits band-stop properties with a very narrow bandwidth that can be represented by a series LC network connected across the transmission line where the values of inductance (L) and capacitance (C) are determined by the length of the dipole and the inter-element distance, respectively. Typically, the inter-element distance is kept low (i.e. $< 0.5\lambda$) to avoid grating lobes (12).

The values of the lumped components are determined by first calculating the Z_{FSS} of the equivalent circuit model (Fig. S8) and setting it equal to zero:

$$Z_{FSS} = jL\omega + \frac{1}{jC\omega} = 0$$
$$\omega_r = \frac{1}{\sqrt{LC}} \qquad [S14]$$

where, ω_r is the central design (resonant) frequency. Next, we use the full-wave simulator to determine the null in Z_{FSS} (ω_r) and set $C = 1/(L\omega_r^2)$. This would ensure that the equivalent-circuit model has the same resonant frequency as the full-wave simulation and only differs in bandwidth. As a result, initial value of L is not important and the bandwidth is optimized by iteratively varying the value of L such that the overall equivalent-circuit response has the minimum Euclidean distance from the full-wave simulation. For this purpose, two frequency points on the lower and higher edges of the -10dB bandwidth were sufficient for good agreement of equivalent-circuit model and simulation results.

Similarly, the model can be extended to multi-layer structures where each additional layer is equivalent of adding similar LC networks in parallel (with a series transmission line indicating the gap between the layers) to the network shown in Fig. S8(A), which results in higher-order filters that means wider filtering frequency bandwidth. As an example, the equivalent circuit of a three-layer FSS is shown in Fig. S8(B) where d_1 and d_2 represent an equivalent transmission (delay) line whose value depends on the inter-layer distance (Δh) between the three layers. the electromagnetic response of each layer can be represented by an equivalent LC network.

6. Dipole position

A. Dipoles along the V-shaped creases. The unique feature of printing dipoles on the mountain creases is that in this configuration, the electrical length and the inter-element distances between the dipoles (along y-axis) varies linearly. This results in a very systematic, predictable and quantifiable frequency response. On the other hand, Miura geometry does not allow comparable linear shrinkage in the y-axis that would result in wider inter-element distances as the Miura geometry is folded. Therefore, the dipoles printed on the V-shaped creases may have a reduced electrical length but inter-element distances would become larger than the λ (wavelength of the operational frequency) with folding. This means that the real and imaginary part of the dipole impedance will change for different values of angle of incidence (as compared to only real part variation in the mountain fold dipoles presented in the paper) resulting in an unstable angle of incidence rejection.

Second, the shape of the dipole on the V-shaped creases is also critical. Let's consider the two sub cases below

A.1. Straight dipoles. In this case, the dipoles are printed along the V-mountain folds of the Miura geometry that are parallel to the x-axis as shown in Fig. S9(A). In the folded configuration, the dipole on the mountain fold folds upwards while the one on the valley fold, folds inwards that would mean that they would experience different phases from the incoming field. The phase variation would become even more pronounced at lower values of the folding angle θ where dipoles would have reduced electrical length (higher resonant frequency) and wider inter-element distances. Thereby further complicating quantification of the electromagnetic behavior of the FSS structure. The non-linearity of such FSS can be seen in Fig. S9(C), where the

resonance frequency at $\theta = 60°$ is lower than the one at $\theta = 90°$ even though the electrical length of the dipole is shorter for the former case. Moreover, the change in resonance frequency with folding angle is also not linear. Last, the bandwidth also decreases with folding which is primarily due to the wider inter-element distances (12). As mentioned earlier, the wider inter-element distances give rise to an unstable angle of incidence rejection as shown in Fig. S9(E,G) for $\theta = 180°$ and $120°$, respectively.

A.2. V-shaped dipoles . In order to minimize the phase difference of the two dipoles at the two folds, a V-shaped dipole can be used as shown in Fig. S9(B). This can introduce linear variation in the frequency response of the Miura-FSS with folding angle as shown in Fig. S9(D). However, inter-element distance (along y-axis) is still much larger for the given dipole length used in the paper and it becomes even larger (compared to resonant frequency wavelength) as the structure is folded. This results in unstable frequency response with angle of incidence (12) as shown in Fig. S9(F,H).

As a conclusion, one of the limitations of Miura structure is that it does not realize linear shrinkage in both axes. This can be realized by using more complex origami structures such as egg-box. However, egg-box cannot be transitioned into flat configuration that makes printing complicated. Therefore, analysis of a dipole-FSS (with dipole placed on the mountain fold) frequency response gives an in-detail and accurate basis to design any tunable FSS using a given origami structure.

B. One dipole on V-shaped crease and one parallel to y-axis. In view of the detailed explanation on the effects of inter-element distance on the FSS frequency response, we can conclude that if we place one dipole on V-shaped crease and one parallel to y-axis neither of them would have required inter-element distance and thus would also have narrow-band and unstable angle of incidence frequency response.

7. Specimens sensitivity

Variation in frequency response due to change in folding angle is the key to realize continuous-range frequency tunability for the proposed structure. Therefore, a quantitative measure of tolerance due to variation of folding angle across the sample is important. Typically, the complete frequency response of FSS structures is defined by both its resonance frequency and the bandwidth. For our structures (band-stop filters), maximum reflection occurs at the resonance frequency while the bandwidth is defined at the two points where the transmission curve intersects the -10dB level. That is the structure reflect at least 90% of the incident power at all frequencies points within the bandwidth of the filter. Thus, a slight shift in resonant frequency can be compensated as long as the desired resonant frequency is within its bandwidth. For example, lets consider the frequency response of a typical single-layer bandstop filter with resonance frequency f_c as shown in Fig. S10(A) with the respective bandwidth highlighted in grey. Now if the resonant frequency shifts at f_2 we can still get good reflection as f_c lies within the (shifted) bandwidth. However, this would not be the case if the resonant frequency shifts to f_1 as value of S_{21} for f_c is more than -10dB. Therefore, the system can compensate for the shift in resonant frequency as long as its magnitude is less than -10dB. That is why very narrow band FSS are generally undesirable because it would not only require a system with very high frequency resolution (thereby increasing its cost) but would also be prone to failure with slight variation in the structure.

In order to quantify the tolerances for the proposed structure with respect to variation in folding angle long the Miura-FSS structure, we fabricated a graded Miura-Ori (13) with dipole elements. The grading allows for a Miura-FSS with different folding angles across the unit cell. We use the intrinsic parameter c (see Fig. S10(B)) to define the grading as follows

$$c_i = (1 + (i-1)P)c_1, \quad i = 1..N \qquad [S15]$$

where i refers to the numbering of the unit cells in the x-direction, N is the total number of unit cells in the x-direction and P is the percentage of increasing. We prototype and tested models with $P = 0.02$ and $P = 0.1$ (i.e., 2% and 10% graded). We design the structure such that all the unit cells have different extension w_i in the x-direction and the same dimension ℓ, v, and h (see Figure S1). This results in the following design constraints

$$\alpha_i = \cos^{-1}\left(\frac{b_1}{b_i} cos(\alpha_1)\right), \quad i = 1..N \qquad [S16]$$

where $\alpha_1 = 45°$, $a = 20$ mm, $b_1 = 20$ mm, and $b_i = (c_1^2 + c_i^2 - b_1^2)^{1/2}$.

The folding angle of all the unit cells is defined as a function of the folding angle θ_1 of the smallest unit cell (i.e., unit cell number 1)

$$\theta_i = \sin^{-1}\left(\sin(\rho)\frac{\sin(\alpha_1)}{\sin(\alpha_i)}\right), \quad i = 1..5 \qquad [S17]$$

where

$$\rho = \cos^{-1}\left(\frac{\sin(\theta_i/2)\cos(\alpha_1)}{(1 - (\sin(\alpha_1)\sin^2(\theta_1/2))^{1/2}}\right) \qquad [18]$$

The simulated and measured results of 0% (uniform Miura-FSS), 2% and 10% graded Miura-FSS are shown in Fig. S10(D) with folding angle $\theta_1 = 90°$. It can be seen that the resonant frequency for uniform (0% graded) Miura-FSS can be filtered even if folding angle of each neighboring cell varies up to 10%.

8. Applications of shape-reconfigurable Miura-FSS

Shape-reconfigurable Miura-FSSs are good candidates for terrestrial, outer-space and electromagnetic cloaking applications over tunable frequency ranges, as well as morphing devices. Reconfigurable FSS allows a designer to use the same structure for different operational frequencies. This also helps re-tune the frequency response of the structure effectively compensating for manufacturing or installation errors or failure of some radiating elements due to environmental factors. One of the most common methods to achieve reconfigurability is to use electronic components such as diodes and varactors that become expensive and complicated for increasing sizes of the FSS structure. Since these are non-linear devices, they make the overall response of the structure non-linear as well. Therefore, Miura-FSS presents a more robust mechanism to change, on-the-fly, the electromagnetic response of FSS structures without using any non-linear electronic components.

In addition to the electromagnetic reconfigurability of Miura-FSS structures, their ability to be stowed in small spaces and on-demand deployability makes them extremely important for terrestrial and outer-space applications. For example, one of the key components of the space-to-ground communication systems is the parabolic reflector that ensures high signal fidelity due to its large gain. However, its typically large size and high manufacturing cost makes it a very expensive payload especially for modern cubesats. That is why modern satellites use reflectarrays due to their planar design and ability to reflect the desired band of frequencies in a given direction. The operation principle of reflectarrays is similar to FSS except that the size of each neighboring element of a reflectarray is varied such that there is a progressive phase difference between them as opposed to FSS where the phase difference is constant between each neighboring element (14). The amount of phase difference dictates the beam scanning ability of the reflectarrays. One of the key drawbacks of these structures is their inability to reconfigure the size of each element on-the-fly thereby limiting its beam scanning ability. On the contrary, the proposed Miura-FSS would enable us to change the size of these radiating elements on-demand by simply changing its folding angle. This would allow us to realize a deployable reflectarray with wider beam scanning ability and lower failure rate as compared to traditional reflectarrays.

Similarly, FSS structures are also used for electromagnetic cloaking of metallic structures. A common figure of merit to detect the electromagnetic size of RF structures (such as antennas) for a given band of frequencies, is its radar cross-section (RCS). Typically, RCS of an antenna is reduced by either placing FSSs at the aperture (of horn antenna) or using them as a ground plane (for planar antennas e.g. patch antenna) (15). The frequency band can be varied by using tunable FSS structures. However, traditional flat FSSs are harder to mount, complicated to reconfigure and additional biasing network for electronic reconfigurable FSS structures may not be desirable for some applications (16). Since Miura-Ori geometry provides higher mechanical strength as well as wider frequency tunability range as compared to flat FSS, the presented Miura-FSS structures would be a better alternative in a sandwich configuration (17). Moreover, multi-layer configuration is typically required for wide-band RCS reduction applications, which is much easier to realize using the approach presented in this work than the traditional multi-layer FSSs.

Another key application could be the design of a universal “morphing” radome that can be optimized for various operational frequencies without modifying its design. Typical radomes feature a curved or a flat configuration. While the curved radomes are extremely costly to fabricate and harder to mount, the flat radomes (comprising of FSS structures) do not offer high reconfigurability and suffer from non-linear affects mentioned earlier. On the other hand, curved Miura structures can be easily realized by varying the shape of the unit cell. This makes mass-production of radomes possible and with their ability to be stowed in small spaces, they can be transported much easily as compared to the traditional radomes. Similarly, due to their higher mechanical strength and wider frequency tunability, they can be used as the filling material in the dry walls for shielding or structural health monitoring purposes (18) that could find applicability in a variety of scenarios e.g. hospitals, radiation rooms, homes (to create localized wifi zones). From the aforementioned, there is a broad range of applications of shape-reconfigurable Miura-FSS.

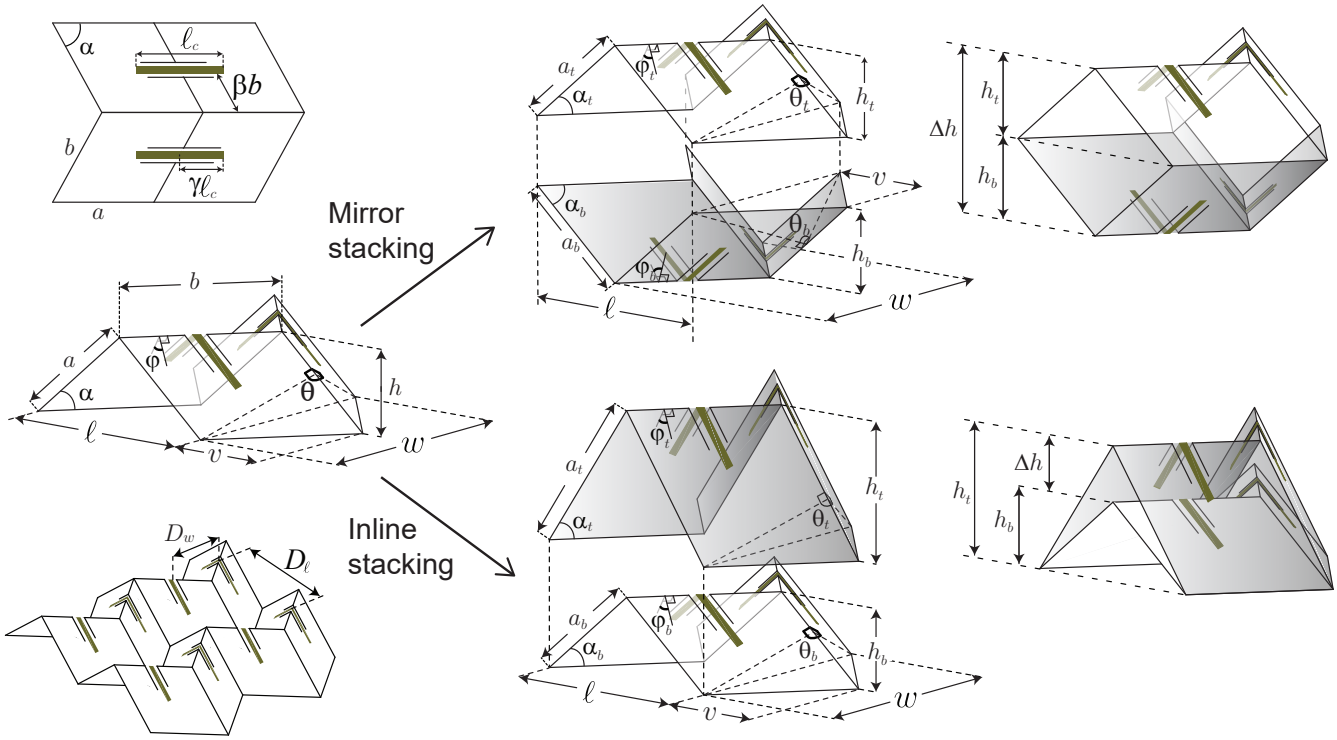

Fig. S1. Schematics of the single- and multi-layer Miura-FSS unit cells.

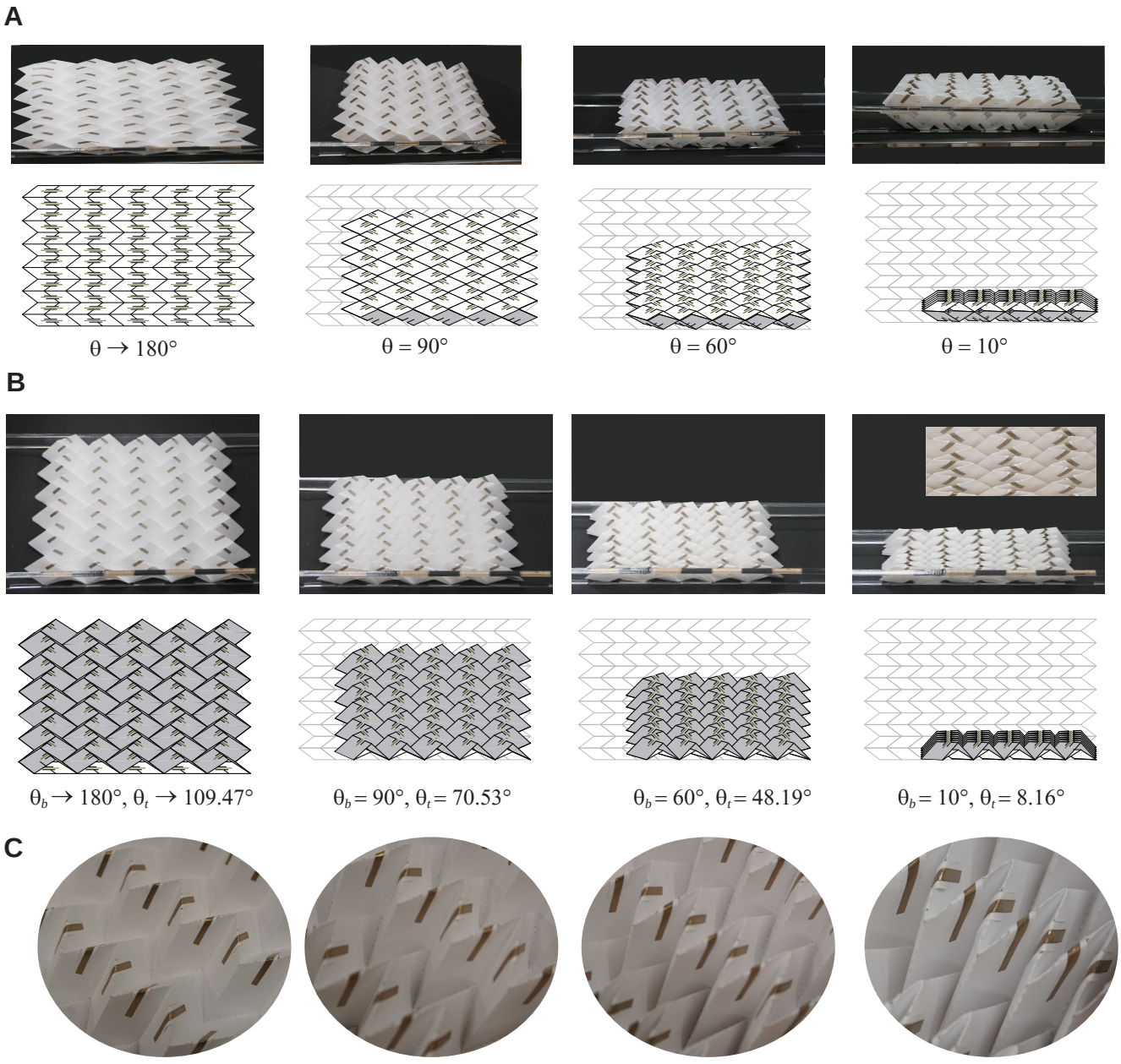

Fig. S2. Illustration of the kinematics of the (A) mirror and (B) inline stacking, and (c) Bridge-like structures in different folding stages.

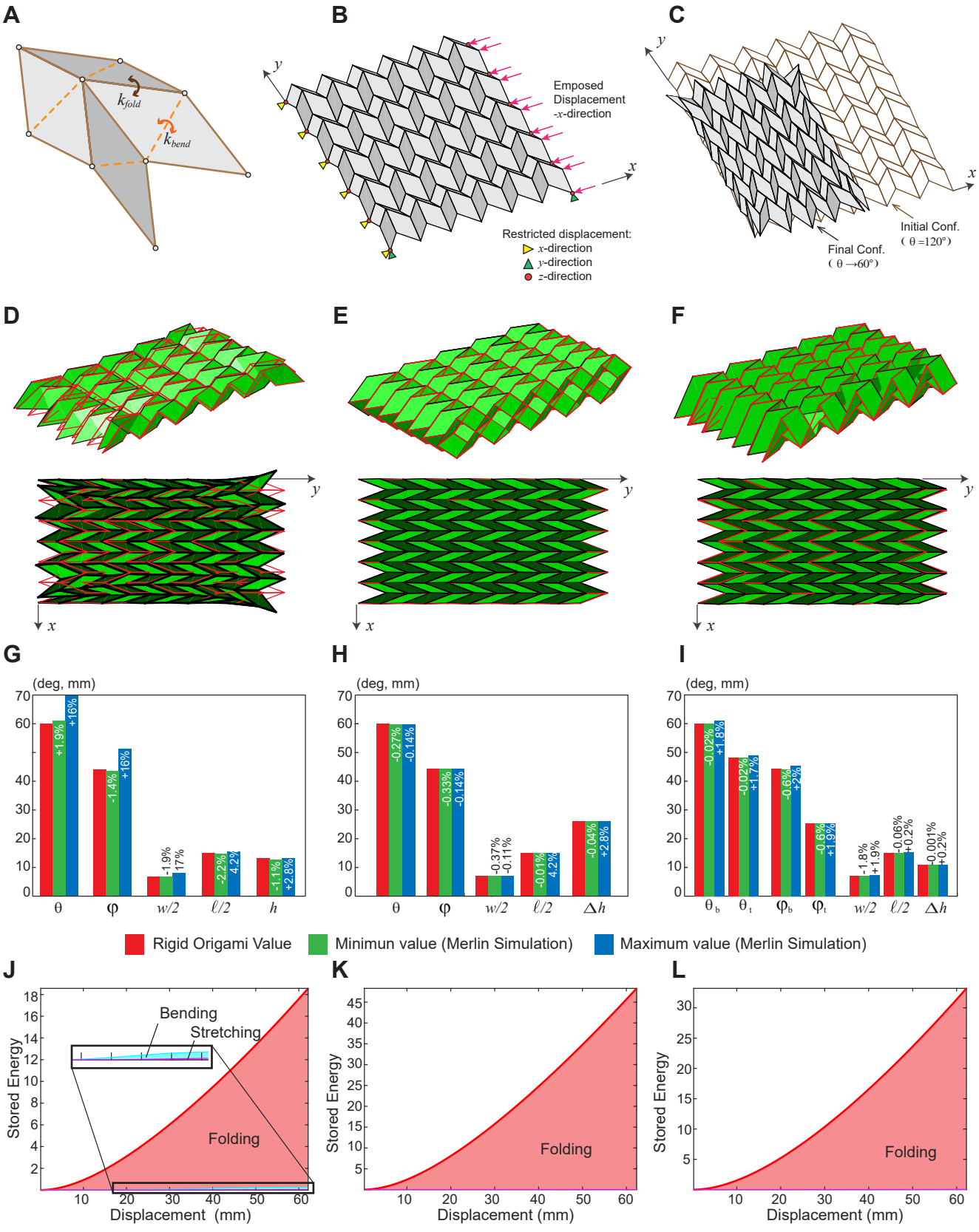

Fig. S3. Mechanical simulation of the Miura-Ori pattern. (A) Discretization of the unit cell using the bar and hinge model. (B) Applied Boundary conditions and (C) final configuration after applied displacement from $\theta = 120^\circ$ to $\theta = 60^\circ$. Final configuration of the (D) single layer and (E) mirror-stacking with $a = b = 20$ mm and $\alpha = 45^\circ$, and (F) inline-stacking with $a_b = b_b = 20$ mm, $\alpha_b = 45^\circ$ and $\alpha_t = 60^\circ$, where the red lines represents the configuration assuming a rigid origami behavior. (G-I) Unit cell parameters comparison with the rigid origami assumption and the maximum and minimum parameters values obtained from the Merlin simulation (J-K) Plot of the stored energy.

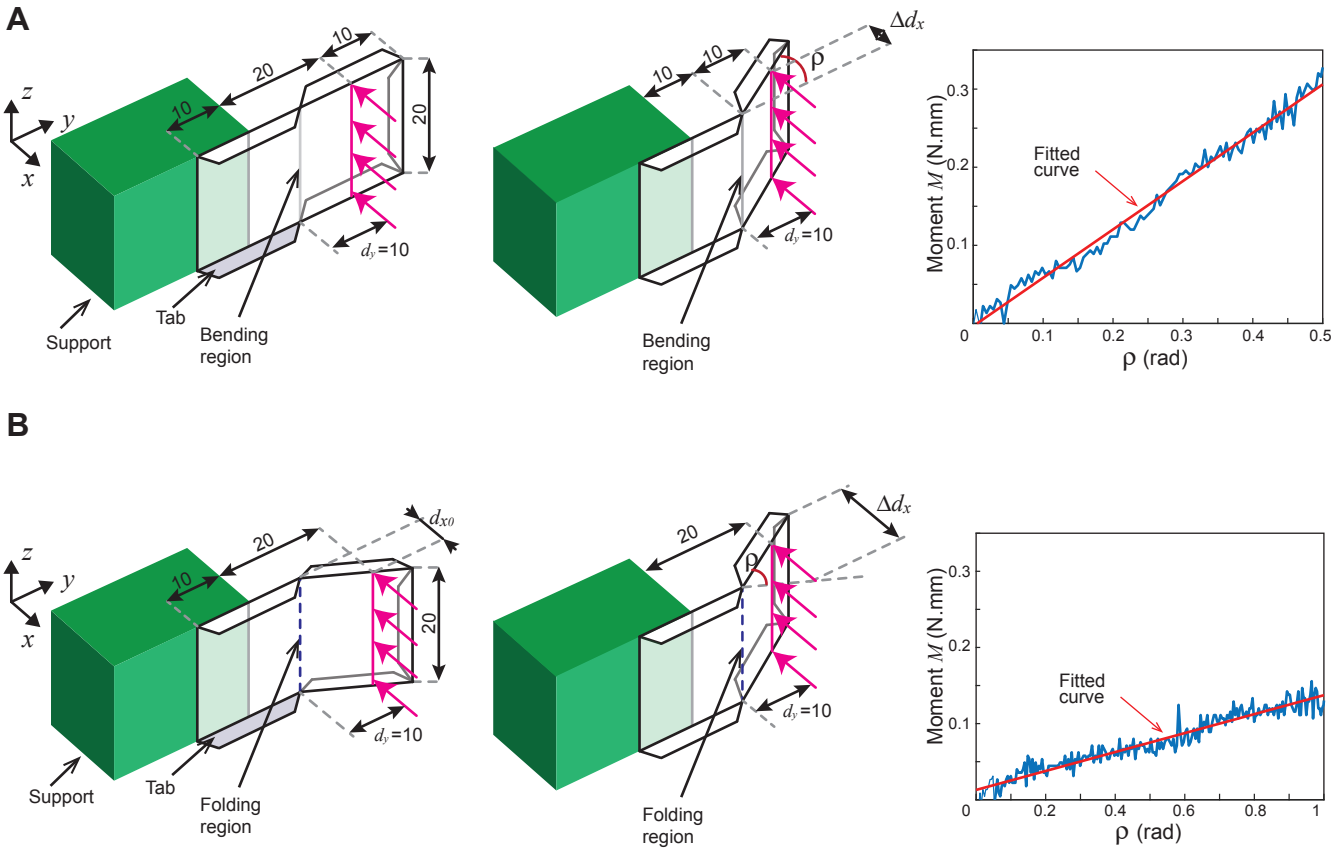

Fig. S4. Illustration of the test setup for stiffness characterization of (A) panel bending and (B) hinge folding, and respective Moment-rotation curve for one sample. The magenta arrows and line represent the region where the displacement is applied.

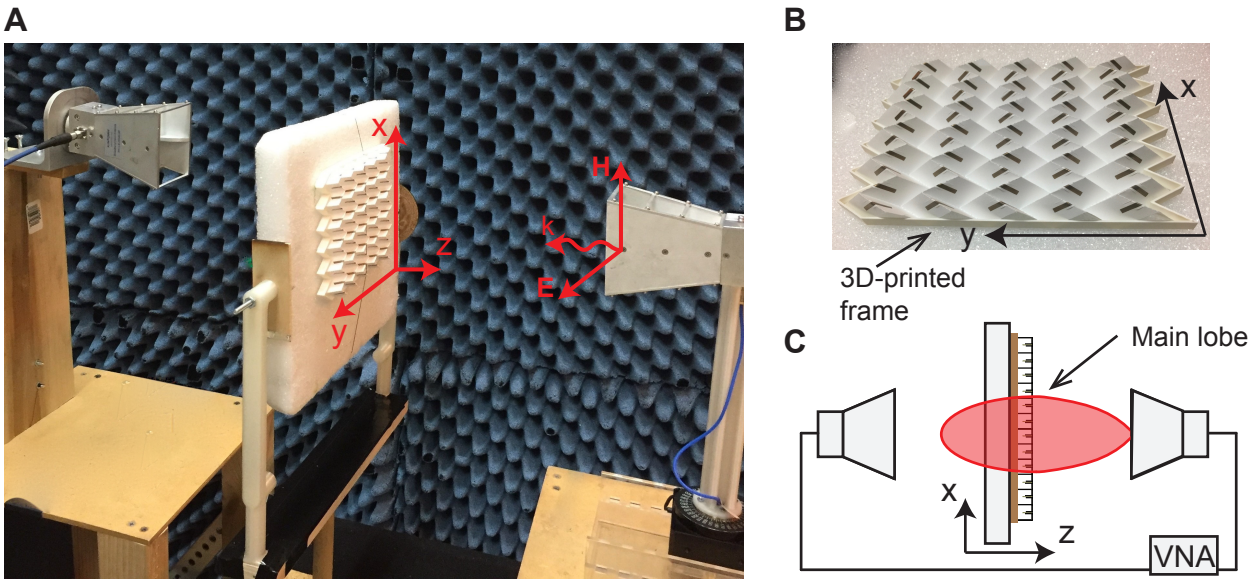

Fig. S5. Experimental setup and prototyped Miura-FSS. (A) Experiment setup, where k, **E**, and **H** are the direction of propagation, the Electric field, and the magnetic field, respectively, of the electromagnetic wave (B) Prototype with the 3d-printed frame (C) Schematics of the position of the prototype relative to the main lobe of the source

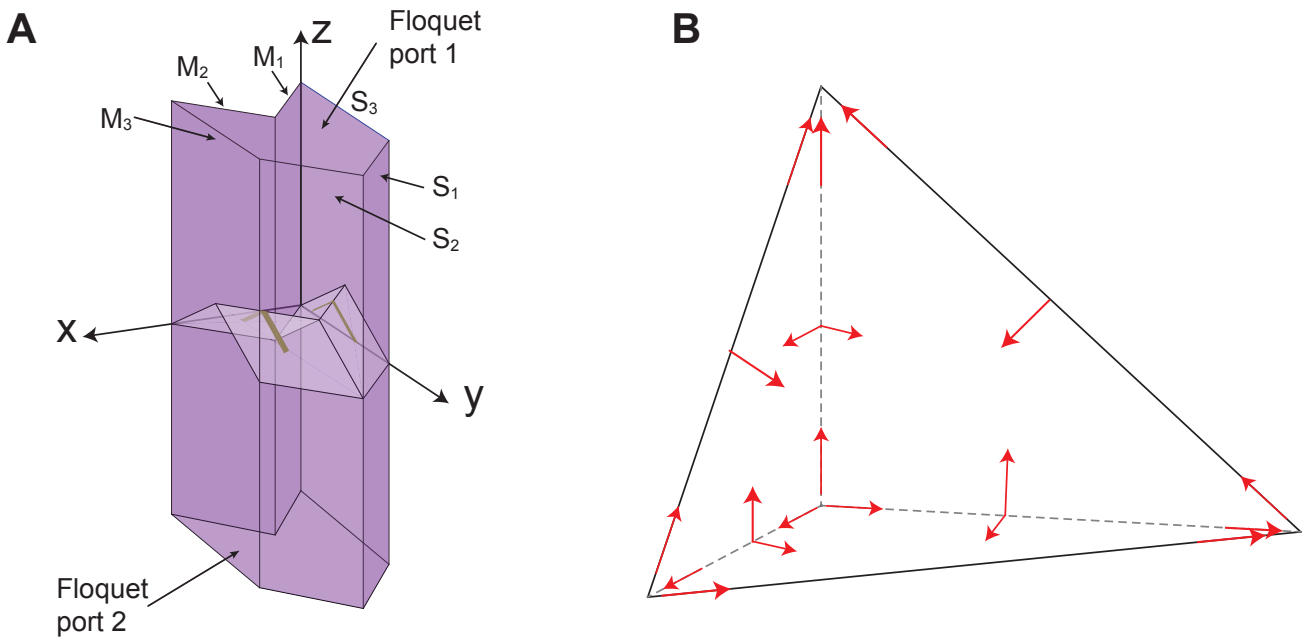

Fig. S6. (A) Numerical model with Floquet port excitation and master-slave boundary condition, where M_i stands for master and S_i for slave and the subscript $i = 1, 2, 3$ identify the master-slave pairs.(B) Tetrahedral element used in the domain discretization

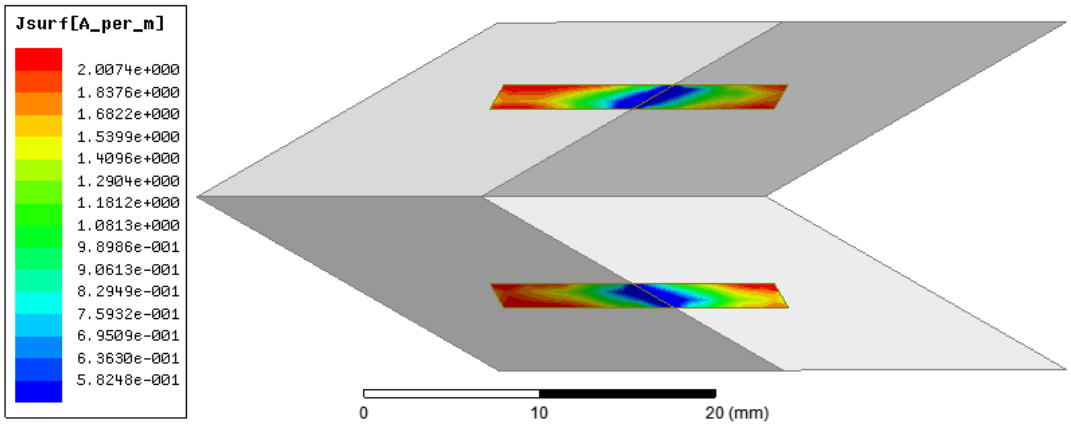

Fig. S7. Surface current density the single-layer Miura-FSS with $\alpha = 45^\circ$ and $\theta = 90^\circ$

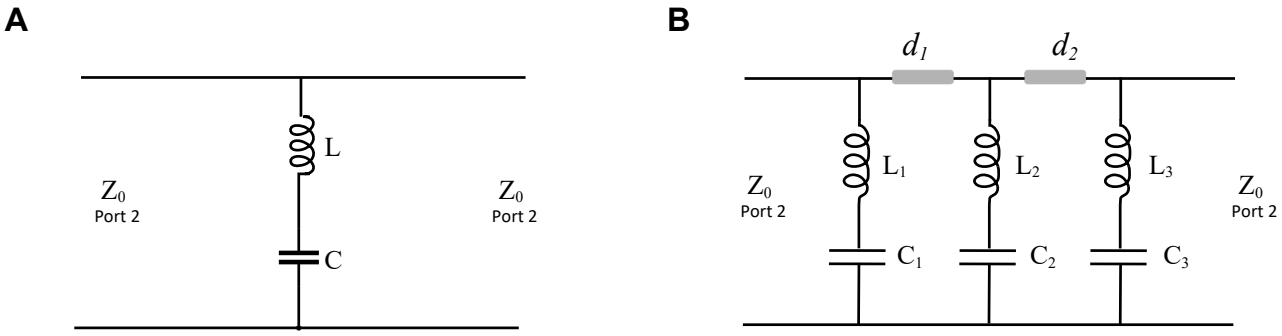

Fig. S8. (A) Equivalent circuit model of single-layer dipole FSS. (B) Equivalent circuit of three layered Miura-FSS with inter-element distances d_1 and d_2.

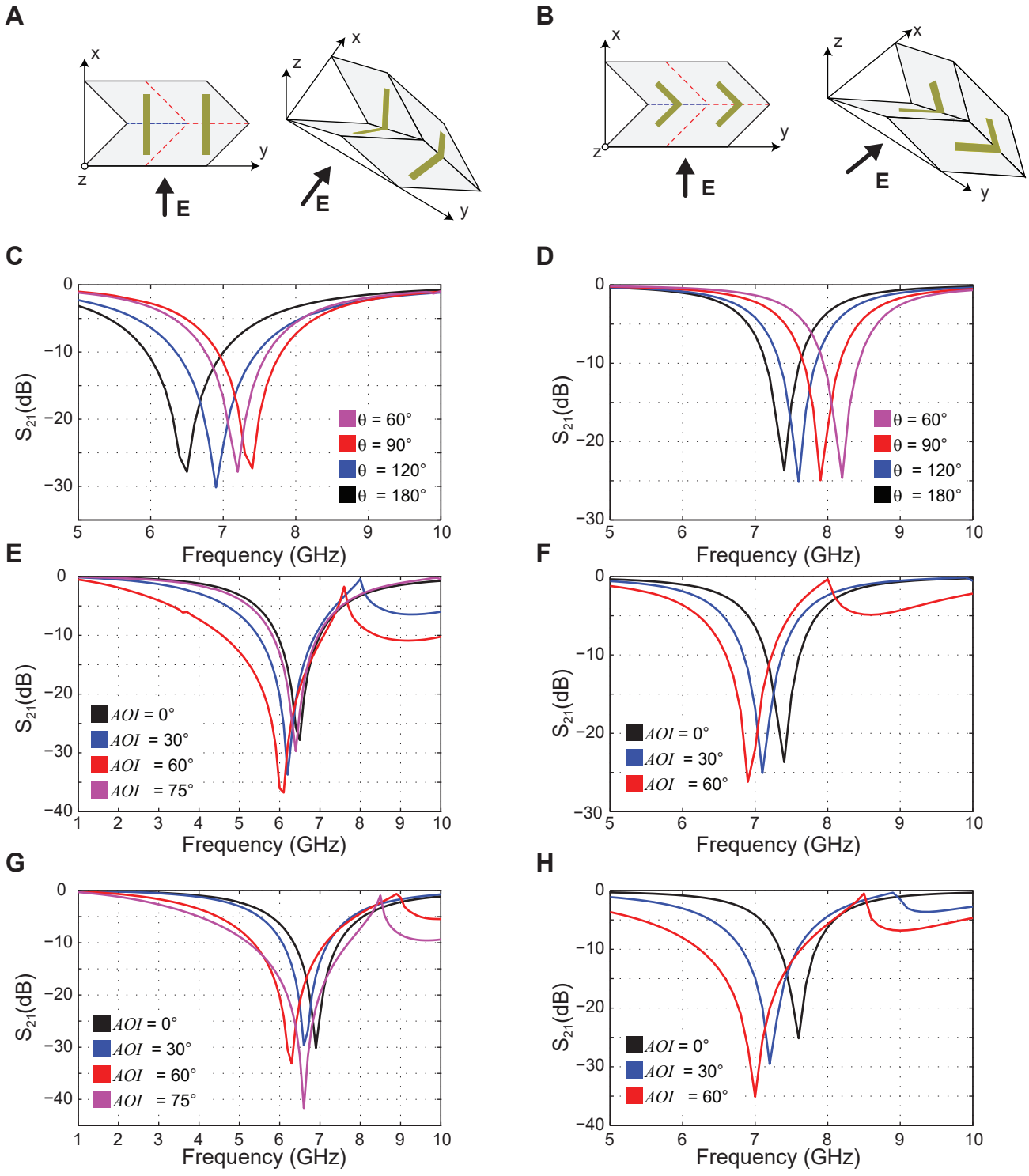

Fig. S9. Unit cell of single-layer Miura-FSS with (A) straight and (B) V-shaped dipoles placed along the V-crease mountain fold in unfolded and folded configuration ($\alpha = 45^\circ$, $a = b = 20$ mm). Simulated S_{21} frequency response for single-layer Miura-FSS with (C) straight and (D) V-shaped dipoles for different values of folding angle θ. Simulated S_{21} frequency response for Miura-FSS with (E,G) straight and (F,H) V-shaped dipoles for different values of angle of incidence (AoI) at flat configuration $\theta = 180^\circ$ and folded configuration $\theta = 120^\circ$, respectively.

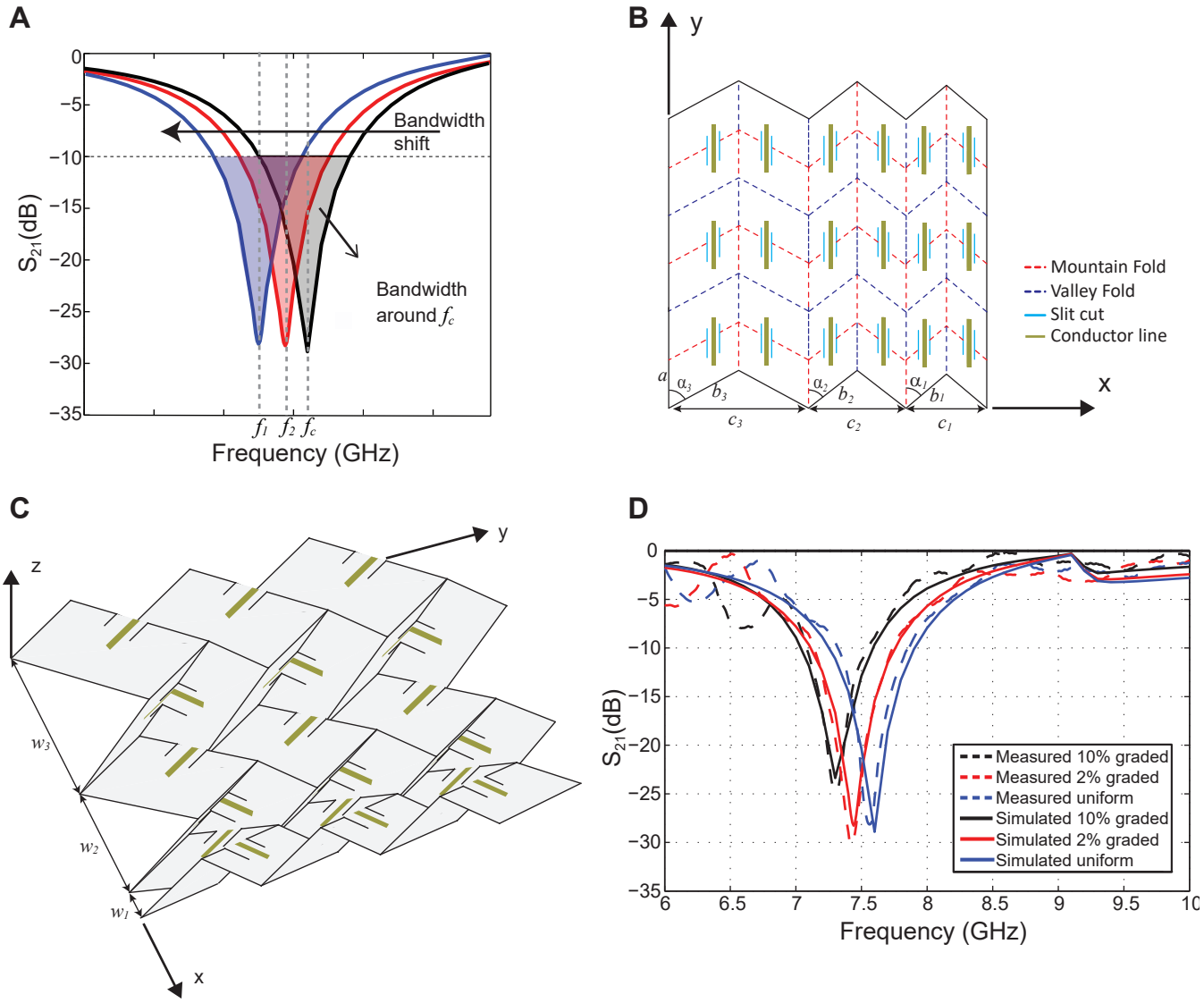

Fig. S10. (A) Schematics of the sensitivity of band-stop filters, (B) Crease pattern and (C) Miura-FSS. (D)Simulated S_{21} frequency response for a graded Miura-FSS.

Table S1. Parameters α_t and a_t of the top layer with $b_t = 20$ mm for a kinematic compatibility with a bottom layer with $a_b = 20$ mm, $b_b = 20$ mm, $\alpha_b = 45°$.

α_t	52°	56°	60°	64°	70°
a_t	22.97 mm	25.29 mm	28.28 mm	32.26 mm	41.35 mm

Table S2. Paper properties: Rotational stiffness of the panels k_{bend} and hinges k_{fold}

k_{bend} (N*mm/rad/mm)	R^2_{fold}	k_{fold} (N*mm/rad/mm)	R^2_{fold}
0.02432	0.9800	0.01211	0.8734
0.02604	0.9417	0.00602	0.8926
0.02533	0.9631	0.00622	0.9212
0.02630	0.9707	0.01263	0.8959
0.02497	0.9536	0.00478	0.8713
Average			
0.025391	0.96182	0.008353	0.89088

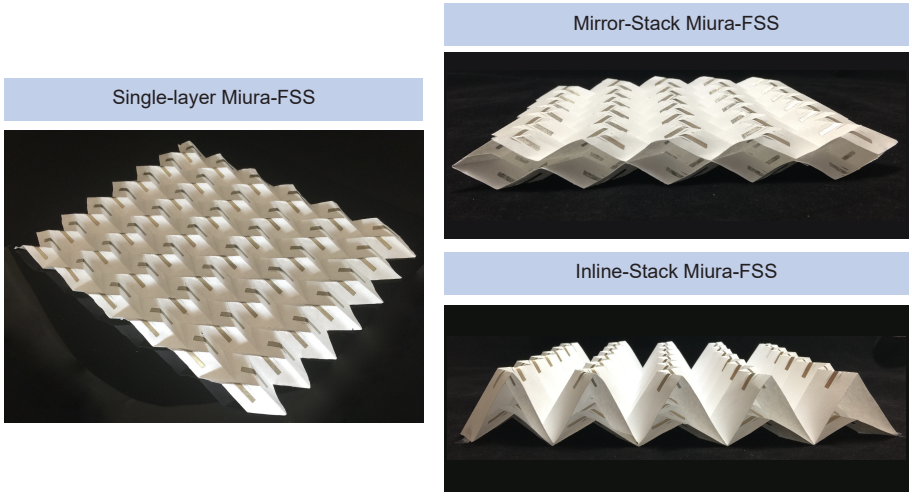

Movie S1. Miura-FSS Prototypes

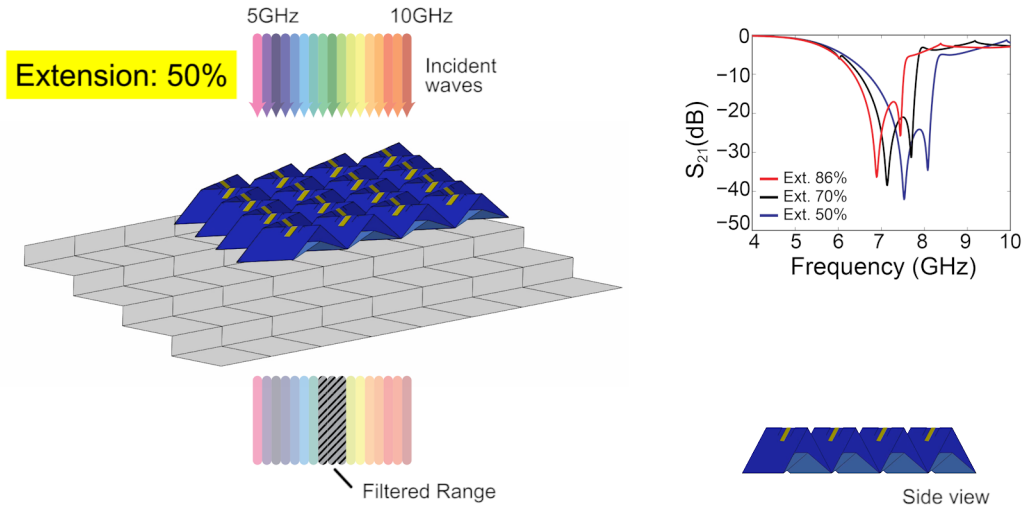

Movie S2. Schematics of the inline-stack Miura-FSS

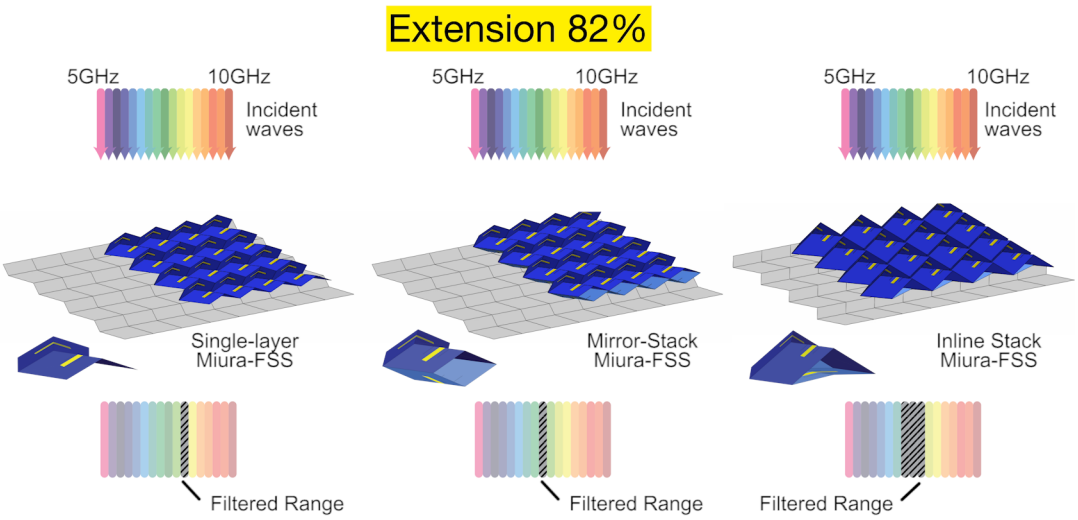

Movie S3. Schematic comparison of the response of the single-layer, mirror-stack, and inline-stack Miura-FSS

Movie S1. Miura-FSS Prototypes

Movie S2. Schematics of the inline-stack Miura-FSS

Movie S3. Schematic comparison of the response of the single-layer, mirror-stack, and inline-stack Miura-FSS

References

1. Wei ZY, Guo ZV, Dudte L, Liang HY, Mahadevan L (2013) Geometric mechanics of periodic pleated origami. *Physical review letters* 110(21):215501.
2. Schenk M, Guest SD (2013) Geometry of miura-folded metamaterials. *Proceedings of the National Academy of Sciences* 110(9):3276–3281.
3. Klett Y, Middendorf P (2016) Kinematic analysis of congruent multilayer tessellations. *Journal of Mechanisms and Robotics* 8(3):034501.
4. Schenk M, Guest SD (2011) Origami folding: A structural engineering approach in *Origami 5: Fifth International Meeting of Origami Science, Mathematics, and Education*. (CRC Press, Boca Raton, FL), pp. 291–304.
5. Liu K, Paulino GH (2017) Nonlinear mechanics of non-rigid origami: an efficient computational approach. *Proc. R. Soc. A* 473(2206):20170348.
6. Liu K, Paulino GH (2016) MERLIN: A MATLAB implementation to capture highly nonlinear behavior of non-rigid origami in *Proceedings of IASS Annual Symposia*. (International Association for Shell and Spatial Structures (IASS)), Vol. 2016, pp. 1–10.
7. Liu K, Paulino GH (2018) Highly efficient nonlinear structural analysis of origami assemblages using the MERLIN2 software in *Origami 7: Seventh International Meeting of Origami Science, Mathematics, and Education*. (Tarquin), Vol. 4, pp. 1167–1182.
8. Munk BA (2003) *Finite antenna arrays and FSS*. (John Wiley & Sons).
9. Lambea M, Gonzalez M, Encinar J, Zapata J (1995) Analysis of frequency selective surfaces with arbitrarily shaped apertures by finite element method and generalized scattering matrix. *Antennas and Propagation Society International Symposium, 1995. AP-S. Digest* 3:1644–1647.
10. Maci S, Cucini A (2006) FSS-based EBG surfaces. *Metamaterials: Physics and Engineering Explorations*.
11. Maci S, Caiazzo M, Cucini A, Casaletti M (2005) A pole-zero matching method for EBG surfaces composed of a dipole FSS printed on a grounded dielectric slab. *IEEE Transactions on Antennas and Propagation* 53(1):70–81.
12. Munk BA (2000) *Frequency selective surfaces: theory and design*. (Wiley Online Library) Vol. 29.
13. Xie R, Li J, Chen Y (2015) The graded origami structures in *ASME 2015 International Design Engineering Technical Conferences and Computers and Information in Engineering Conference*. (American Society of Mechanical Engineers), pp. V05BT08A026–V05BT08A026.
14. Pozar D, Metzler T (1993) Analysis of a reflectarray antenna using microstrip patches of variable size. *Electronics Letters* 29(8):657–658.
15. Luo GQ, et al. (2007) Filtenna consisting of horn antenna and substrate integrated waveguide cavity fss. *IEEE transactions on antennas and propagation* 55(1):92–98.
16. Ferreira D, Cuiñas I, Caldeirinha RF, Fernandes TR (2017) 3-d mechanically tunable square slot fss. *IEEE Transactions on Antennas and Propagation* 65(1):242–250.
17. Klett Y, Middendorf P, Sobek W, Haase W, Heidingsfeld M (2017) Potential of origami-based shell elements as next-generation envelope components in *Advanced Intelligent Mechatronics (AIM), 2017 IEEE International Conference on*. (IEEE), pp. 916–920.
18. Jang SD, Kang BW, Kim J (2012) Frequency selective surface based passive wireless sensor for structural health monitoring. *Smart Materials and Structures* 22(2):025002.